8258–8270 *Nucleic Acids Research, 2011, Vol. 39, No. 18* *Published online 4 July 2011*
doi:10.1093/nar/gkr314

Modulation of the stability of the *Salmonella* fourU-type RNA thermometer

Jörg Rinnenthal[1], Birgit Klinkert[2], Franz Narberhaus[2] and Harald Schwalbe[1,*]

[1]Institute for Organic Chemistry and Chemical Biology, Center for Biomolecular Magnetic Resonance, Johann Wolfgang Goethe-University, Max-von-Laue-Strasse 7, D-60438 Frankfurt/Main and [2]Microbial Biology, Ruhr-Universität Bochum, Universitätsstrasse 150, NDEF06/783, 44780 Bochum, Germany

Received February 9, 2011; Revised and Accepted April 19, 2011

ABSTRACT

RNA thermometers are translational control elements that regulate the expression of bacterial heat shock and virulence genes. They fold into complex secondary structures that block translation at low temperatures. A temperature increase releases the ribosome binding site and thus permits translation initiation. In fourU-type RNA thermometers, the AGGA sequence of the SD region is paired with four consecutive uridines. We investigated the melting points of the wild-type and mutant sequences. It was decreased by 5°C when a stabilizing GC basepair was exchanged by an AU pair or increased by 11°C when an internal AG mismatch was converted to a GC pair, respectively. Stabilized or destabilized RNA structures are directly correlated with decreased or increased *in vivo* gene expression, respectively. Mg^{2+} also affected the melting point of the fourU thermometer. Variations of the Mg^{2+} concentration in the physiological range between 1 and 2 mM translated into a 2.8°C shift of the melting point. Thus, Mg^{2+} binding to the hairpin RNA is regulatory relevant. Applying three different NMR techniques, two Mg^{2+} binding sites were found in the hairpin structure. One of these binding sites could be identified as outer sphere binding site that is located within the fourU motif. Binding of the two Mg^{2+} ions exhibits a positive cooperativity with a Hill coefficient of 1.47. Free energy values ΔG for Mg^{2+} binding determined by NMR are in agreement with data determined from CD measurements.

INTRODUCTION

The maintenance of the intracellular metal ion concentration is an indispensable requirement for the viability of eukaryotic and prokaryotic cells. Cells exhibit high intracellular K^+ and Mg^{2+} concentrations while cytosolic Na^+ and especially Ca^{2+} concentrations are kept low (1). By varying the K^+ concentration, cells adopt the intracellular to the extracellular osmolality (2). K^+ acts as counterion for nucleic acids (DNA, RNA) (3,4) and has been found to stabilize the structure of cytosolic proteins. Mg^{2+} is prominent for binding and activating ATP (5) as well as intracellular enzymes (1). In addition to K^+, it is the most important cation acting as counterion of nucleic acids (1,4). It is involved in the maintenance of the structural integrity of the plasma membrane (6) and stabilizes proteins. In gram-negative bacteria, Mg^{2+} binding to lipopolysaccharides stabilizes the periplasmic membrane (7). Most importantly, it is strictly required for rRNA folding, ribosome assembly and ribosome function (8,9).

The importance of Mg^{2+} ions for the viability of prokaryotic cells has some important implications. First, Mg^{2+} starvation leads to growth arrest of bacterial cultures (10). Second, although the amount of Mg^{2+} within a prokaryotic cell may vary by a factor of three, the RNA[kg]:Mg^{2+}[kg] ratio ($\approx$68) is almost constant under differing environmental conditions (10). *Escherichia coli* cells that enter the stationary phase reduce the concentration of ribosomes and thus reduce their Mg^{2+} content (11). Third, *E. coli* cells react on Mg^{2+} starvation by the synthesis of polyamines including spermidine and putrescine which are able to substitute for Mg^{2+} in many cases. For instance, the spermidine/Mg^{2+} ratio bound to the ribosomal fraction of *E. coli* cells reduces with increasing extracellular Mg^{2+} concentration (12). Due to the diversity of different Mg^{2+} binding partners and the multitude of different intracellular Mg^{2+} binding sites, most of the intracellular Mg^{2+} is present in a bound form, albeit transiently. *E. coli* cells in the exponential growth phase have a Mg^{2+} content of 90–110 mM (13), while only a small fraction of 1–2 mM is present in the physiologically active free form (14). In addition, most of the bound Mg^{2+} fraction is in fast exchange with the free Mg^{2+} in the cytosol (14,15) and a 20–30% loss of Mg^{2+} is sufficient for cell-growth arrest (14). Due to this rapid exchange between free and bound Mg^{2+}, also the

*To whom correspondence should be addressed. Tel: 69 7982 9737; Fax: 69 7982 9515; Email: schwalbe@nmr.uni-frankfurt.de

concentration of the free form has to be controlled tightly by the cell itself to assure cell viability. Indeed, Mg^{2+} ions have been found to be actively transported among others in *E. coli* (15–19), *Bacillus subtilis* (20) and *Salmonella typhimurium* (21) and the Mg^{2+} transport mechanisms of *S. typhimurium* and *E. coli* are equivalent to each other (1,14,18,21–25).

Ions are important for stabilizing RNA tertiary structure (3,9,26). Most often, K^+ and Mg^{2+} cations serve this task although Mn^{2+} ions and polyamines such as spermidine have the potential to substitute for some of the K^+ and Mg^{2+} binding sites. Mn^{2+} ions are able to substitute for 76% of the bound Mg^{2+} ions in *E. coli* without impairing viability of the cells (18). These findings provide support for using Mn^{2+} ions to map Mg^{2+} binding sites within an RNA molecule (27–30).

Due to its small size and divalent charge, the Mg^{2+} ion has a notably high charge density. Therefore, the first water hydration sphere is more stable than for any other physiologically relevant cation (31). Mg^{2+} coordinates six water molecules with octahedral geometry. Mg^{2+} ions are able to bind to RNA with different binding modes. Generally, 'inner sphere' and 'outer sphere' contacts can be distinguished (9). In an 'outer sphere' complex, water molecules of the $Mg(H_2O)^{2+}{}_6$ complex but not the Mg^{2+} ion itself make contacts to the functional groups of the RNA. In contrast, inner sphere contacts are characterized by at least one direct contact of the Mg^{2+} ion to functional groups of the RNA. Inner sphere contacts can be classified by the number of inner sphere ligands other than H_2O (type I, type II, type III, etc.), while 'type 0′ is identical to an outer sphere contact (9). Klein *et al.* (9) modeled Mg^{2+} ions into the structure of the large ribosomal subunit from *Haloarcula marismortui* and found that 65% of the bound Mg^{2+} ions are outer sphere coordinated. Within the remaining inner sphere contacts, most contacts belong to the classes type I or type IIa where inner sphere ligands are orthogonally oriented to each other. Most of these Mg^{2+} ions (type I and type IIa) are coordinated to either one or both non-bridging oxygens of the phosphate backbone. Outer sphere coordinated Mg^{2+} ions are most often located within the major groove of the RNA helices and make indirect, water-mediated contacts to the heteroatoms of the nucleobases (9,27,32).

Mg^{2+} has a profound effect on the structure and function of riboswitches (33–35). Riboswitches are biosensors that control gene expression in response to cellular metabolites that they bind with high affinity and specificity (36,37). RNA thermometers are capable of sensing temperature. They control translation initiation of heat shock and virulence genes by sequestration of the Shine–Dalgarno (SD) sequence at low temperatures (38). At higher temperatures, the hairpin structure melts in a zipper-like manner allowing translation initiation to occur (39). Helix stability in simple synthetic RNA thermometers is directly correlated to gene expression levels of the downstream gene (40).

We recently investigated the structure, function and melting mechanism of the *Salmonella* fourU RNA thermometer, which controls expression of the heat shock gene *agsA* (39,41). In the present work, we examined the *in vitro* and *in vivo* effects of a point mutation that weakens an extraordinarily stable GC base pair, which had been shown to prevent unfolding of the wild-type RNA at lower temperatures (39) (Figure 2). Furthermore, we highlight the Mg^{2+} binding properties of the fourU RNA thermometer. Using NMR spectroscopy, we identified and localized two Mg^{2+} binding sites and determined their dissociation constants as well as the cooperativity between these binding sites. Mg^{2+}-dependent changes in thermal stability of the fourU RNA thermometer were determined by CD spectroscopy. Our study provides first evidence for Mg^{2+} binding of an RNA thermometer and its relevance for RNA thermometer function.

MATERIALS AND METHODS

NMR spectroscopy

NMR measurements were performed on a 600 MHz (14.09 T) Bruker NMR spectrometer equipped with a 5-mm xyz-gradient probe and a 900-MHz (21.14 T) Bruker NMR spectrometer equipped with a 5-mm cryogenic HCN z-gradient probe. Spectra were recorded and processed using the Bruker TopSpin 2.0/2.1 software. Processed spectra were analyzed with Sparky 3.1.1.3.

$MgCl_2$ titration experiments

Mg^{2+} titration experiments of the 4U-hp2-wt RNA were performed in NMR buffer (see RNA preparation section) at a temperature of 10°C. [^{1}H-^{15}N]-HSQC experiments were recorded at a B_0 field strength of 900 MHz (21.14 T) using a standard pulse sequence (42) (Topspin 2.1 pulse program library: fhsqcf3gpph) with a hard Watergate pulse train for water suppression (43). Spectra were recorded with a spectral width of 30 ppm in the ^{15}N-dimension and 22 ppm in the ^{1}H-dimension. A total of 240 increments were recorded in the ^{15}N-dimension and 4096 points in the ^{1}H-dimension. [^{1}H,^{15}N]-HSQC spectra were recorded at the following $MgCl_2$ concentrations: 0, 0.3, 0.5, 0.7, 1.0, 1.5, 2.0, 3, 5 and 7 mM.

Overall chemical shift perturbations (CSPs) were calculated from the CSPs of the ^{15}N and the ^{1}H-dimension (44) according to the following equation:

$$\mathrm{CSP} = \sqrt{\frac{(\mathrm{CSP}_H)^2+(\mathrm{CSP}_N/5)^2}{2}} \quad (1)$$

Since association and dissociation of the Mg^{2+} ions from the target RNA are fast on the NMR timescale, CSPs can be related to the Mg^{2+} concentration within the sample according to the following equation:

$$f(x) = \frac{b}{2} \times \left[(x+1+a) - \sqrt{\left((x+1+a)^2-4x\right)}\right] \quad (2)$$

Equation (2) is derived from the mass action law for an RNA/Mg^{2+} equilibrium with the RNA having one Mg^{2+} binding site. In Equation (2) $f(x)$ is the CSP of an individual imino signal at a given $x = [Mg^{2+}]/[RNA]$ ratio, a is

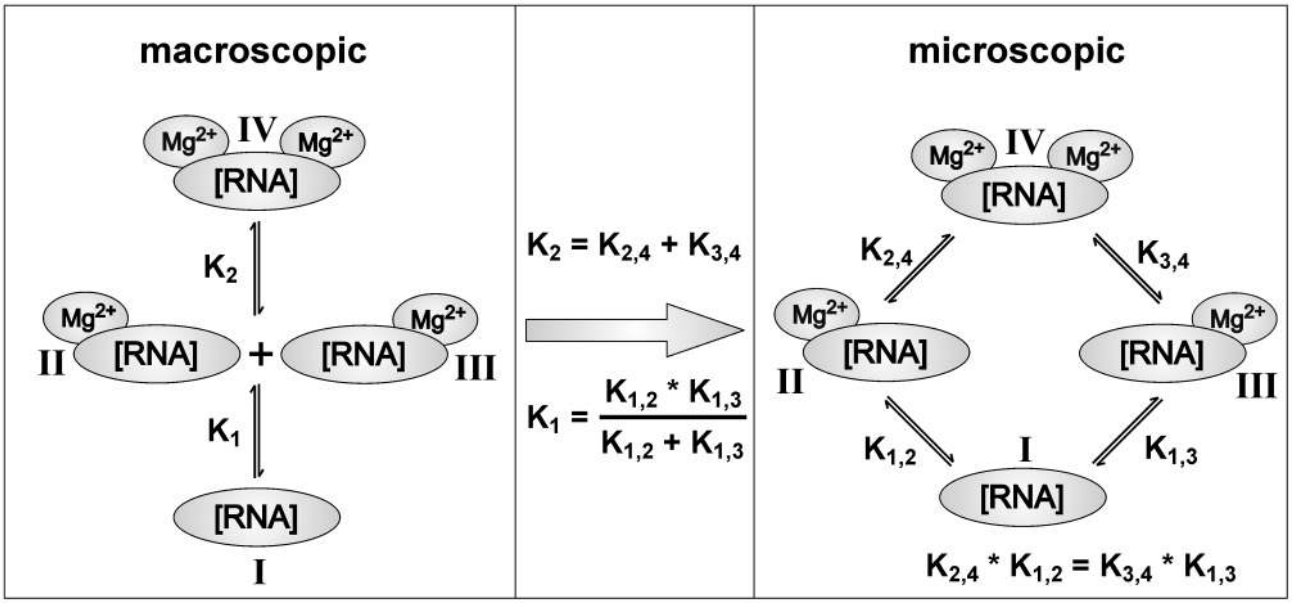

Figure 1. Mg^{2+} binding model assuming two distinct Mg^{2+} binding sites on the RNA. The RNA can adopt four different states (I, II, III, IV). Transitions between these states are described by microscopic dissociation constants ($K_{1,2}$, $K_{1,3}$, $K_{2,4}$, $K_{3,4}$). Transitions between free RNA, binary and ternary complex are described by macroscopic dissociation constants (K_1, K_2). In addition, equations describing interdependencies of the different dissociation constants are given. K_1 and K_2 as well as $K_{1,2}$, $K_{1,3}$, $K_{2,4}$ and $K_{3,4}$ are thermodynamic constants that describe the RNA-$[Mg^{2+}]_n$ complexes under equilibrium conditions.

the ratio between dissociation constant (K_D) and RNA concentration and b is the maximum CSP at infinite Mg^{2+} concentration. During the fitting procedure, the parameters a and b were allowed to adjust freely.

CSP curves that showed biphasic behavior and could not be fitted by Equation (2) were fitted by a model assuming two different binding sites (Figure 1). Such a model is characterized by two macroscopic (K_1, K_2) and four microscopic ($K_{1,2}$, $K_{1,3}$, $K_{2,4}$, $K_{3,4}$) dissociation constants that connect four different RNA states (I, II, III, IV). Considering a particular imino group, two different states with only one Mg^{2+} ion bound (states II and III in Figure 1) can have different or equal (degenerated) chemical shifts. Such model predicts that biphasic curves only depend on the macroscopic dissociation constants K_1 and K_2. Monophasic curves, in contrast, detect either macroscopic or microscopic dissociation constants, depending on which chemical shifts of the four states are degenerated for a particular imino group. Microscopic and macroscopic dissociation constants are related to each other by the equations depicted in Figure 1.

Biphasic CSP curves can be fitted by Equations (3–5), if the two binary complexes have different chemical shifts.

$$\mathrm{CSP} = a^*\theta_{(\mathrm{BA2})} + b^*\theta_{(\mathrm{AB})} \quad (3)$$

$$\theta_{(\mathrm{AB})} = \frac{K_1K_2 \times [\mathrm{A}]}{K_{1,3}(K_1K_2 + K_2[\mathrm{A}] + [\mathrm{A}]^2)} \quad (4)$$

$$\theta_{(\mathrm{BA2})} = \frac{[\mathrm{A}]^2}{(K_1K_2 + K_2[\mathrm{A}] + [\mathrm{A}]^2)} \quad (5)$$

Biphasic CSP curves can be fitted by Equation (5–7), if the complexes [AB] and [BA] are degenerated.

$$\mathrm{CSP} = a^*\theta_{(\mathrm{BA2})} + (b/2)^*\theta_{(\mathrm{AB+BA})} \quad (6)$$

$$\theta_{(\mathrm{AB+BA})} = \frac{K_2 \times [\mathrm{A}]}{(K_1K_2 + K_2[\mathrm{A}] + [\mathrm{A}]^2)} \quad (7)$$

Whether chemical shifts are degenerated in the binary complexes or not, influences only the parameter b in the Equations (3) and (6). In Equations (3) and (4), the constants b and $K_{1,3}$ cannot be fitted independently and can therefore be summarized to one constant.

In Equations (3)–(7), [A] is the concentration of Mg^{2+}-ions, $\theta_{(\mathrm{AB})}$ and $\theta_{(\mathrm{BA})}$ are the populations of the two different binary (RNA^*Mg^{2+})-complexes and $\theta_{(\mathrm{AB2})}$ is the population of the ternary (Mg^{2+}*RNA*Mg^{2+})-complex. Parameters a and b are fitting parameters that modulate the CSP amplitude. K_1, K_2 are the macroscopic and $K_{1,2}$, $K_{1,3}$, $K_{2,4}$, $K_{3,4}$ the microscopic dissociation constants of the Mg^{2+} binding model which assumes two Mg^{2+} binding sites (Figure 1). During the fitting procedure, the parameters a, b, K_1 and K_2 were allowed to adjust freely.

In some cases, three out of four RNA states have degenerated chemical shifts and only one state has a differing chemical shift. For some of these cases, this results in monophasic CSP curves. For example, if state I has a differing chemical shift, the macroscopic dissociation constant K_1 is detected. If state IV has a differing chemical shift from states I, II and III, the macroscopic dissociation constant K_2 is detected. In the special case of equal microscopic dissociation constants ($K_{1,2}$, $K_{1,3}$, $K_{2,4}$,

$K_{3,4}$) the macroscopic dissociation constant K_2 is four times larger than the macroscopic dissociation constant K_1 ($K_2 = 4*K_1$).

$MnCl_2$ PRE experiments

Paramagnetic relaxation enhancement (PRE) effects caused by paramagnetic Mn^{2+} ions were analyzed for the observable imino groups within the 4U-hp2-wt RNA. [^{1}H-^{15}N]-HSQC spectra of the imino region of a 4U-hp2-wt RNA sample were recorded in NMR buffer in the presence of 5 mM $MgCl_2$ at $MnCl_2$ concentrations of 0 and 4 μM. Experiments were performed at a temperature of 10°C and a B_0 field strength of 900 MHz (21.14 T). The recycling delay was set to 3 s. Remaining acquisition parameters were identical to the $MgCl_2$ titration experiments. PRE effects were quantified by intensity and line width analysis. Line width analysis was performed for the indirect ^{15}N-dimension. Intensities and line widths were analyzed with Sparky 3.1.1.3. For the PRE analysis we plotted ln (I[0 μM]/I[4 μM]) for each observable imino signal and compared the results with the change in line width (υ[4 μM] − υ[0 μM]).

$Co(NH_3)^{3+}_6$ NOESY experiment

To identify and localize Mg^{2+} outer sphere binding sites, a NOESY spectrum of a 4U-hp2-wt RNA sample in NMR buffer was recorded in the presence of 5 mM $Co(NH_3)^{3+}_6$. Measurements were performed at a temperature of 10°C and a B_0 field strength of 600 MHz (14.09 T) with a mixing time T_m of 150 ms. The spectrum was recorded with a spectral width of 15 ppm in the indirect dimension and 22 ppm in the direct dimension. A total of 896 increments were recorded in the t_1 dimension and 2048 points in the t_2-dimension. Each increment was recorded with 128 scans.

RNA preparation

Unlabeled and ^{15}N-labeled RNA oligonucleotides were synthesized by *in vitro* transcription with T7 RNA polymerase from linearized plasmid DNA templates and purified as described previously (45). ^{15}N-labeled nucleotides were purchased from Silantes (Munich, Germany), unlabeled nucleotides were purchased from Sigma Aldrich (St. Louis, MO, USA).

RNAs were desalted using Vivaspin 20 concentrators with a molecular weight cutoff (MWCO) of 3000 Da from Sartorius stedim biotech (Aubagne Cedex, France). RNA refolding was achieved by denaturing for 10 min at a concentration of 0.25 mM and a temperature of 95°C followed by 20-fold dilution with ice cold water and subsequent incubation at 0°C for another 30 min. RNAs were concentrated and exchanged to NMR buffer using Vivaspin 20 concentrators (MWCO = 3000 Da). The NMR buffer contained 15 mM $K_xH_yPO_4$ (pH 6.5), 25 mM KCl, 90% H_2O and 10% D_2O. Correct RNA folding was verified by native polyacrylamide gel electrophoresis.

Native gel electrophoresis

The 5× loading buffer was composed of 87% glycerole, 0.1% (w/v) xylene cyanole FF and 0.1% (w/v) bromophenol blue. The 1× running buffer contained 50 mM Tris–acetate and 50 mM sodium phosphate (pH 8.3). Gels were cast using 15% acrylamide with an acrylamide:bisacrylamide ratio of 37.5:1. Running conditions were set as follows: $U = 70$ V, $P < 0.5$ W for 4 h, water cooling to prevent heating. Gels were stained with ethidium bromide.

CD spectroscopy

CD melting and refolding curves were recorded with a JASCO spectropolarimeter J-810 at a wavelength of 258 nm. The RNA concentration was adjusted to 25 μM. Buffer conditions: 15 mM $K_xH_y(PO_4)$, 25 mM KCl, pH 6.5. Melting curves were recorded with a temperature slope of 1°C/min (4U-hp2-wt: 5-90°C; 4U-hp2-G14A-C25U-mutant: 2-80°C; 4U-hp2-A8C-mutant: 10-90°C) and refolding curves with a temperature slope of −1°C/min (4U-hp2-wt: 90-5°C; 4U-hp2-G14A-C25U-mutant: 80-2°C; 4U-hp2-A8C-mutant: 90-10°C). CD melting and refolding curves were normalized according to Equation (9) and thermodynamic parameters (ΔH_{unf}, ΔS_{unf}, ΔG_{unf} and T_m) were derived from Equations (10) to (12).

Assuming the RNA to be either folded or unfolded (two-state model), the fraction of unfolded RNA can be expressed by

$$\alpha(T) = 1 - \frac{[\mathrm{RNA}_{\mathrm{folded}}(T)]}{[\mathrm{RNA}_{\mathrm{total}}]} \quad (8)$$

The fraction of unfolded RNA α is varying with temperature. This temperature dependence of α can be determined from the temperature dependence of the ellipticity at a wavelength of 258 nm according to Equation (9)

$$\alpha(T) = 1 - \frac{\theta(T) - \theta_{\mathrm{unfolded}}(T)}{\theta_{\mathrm{folded}}(T) - \theta_{\mathrm{unfolded}}(T)} \quad (9)$$

In Equation (9), $\theta(T)$ is the measured temperature-dependent ellipticity, $\theta_{\mathrm{unfolded}}(T)$ and $\theta_{\mathrm{folded}}(T)$ are the ellipticities of the unfolded and the folded state of the RNA, respectively. $\theta_{\mathrm{unfolded}}(T)$ and $\theta_{\mathrm{folded}}(T)$ are also slightly temperature-dependent and are therefore approximated linearly. From the resulting $\alpha(T)$ dependence, the molar unfolding enthalpy ΔH_{unf} can be calculated (46) according to Equation (10). The melting point T_m is defined as the temperature at which 50% of the RNA is unfolded ($\alpha = 0.5$). In case of perfect sigmoidality, the slope of the $\alpha(T)$ curve is maximal at this temperature

$$\Delta H_{\mathrm{unf}} = 4RT_m^2 \left(\frac{\partial \alpha}{\partial T}\right)_{T=T_m} \quad (10)$$

In Equation (11), R is the gas constant, T_m the melting temperature, α the fraction of unfolded RNA and ΔH_{unf} the molar unfolding enthalpy of the RNA. From ΔH_{unf}, the molar unfolding entropy ΔS_{unf} can be calculated according to Equation (11)

$$\Delta S_{\mathrm{unf}} = \frac{\Delta H_{\mathrm{unf}}}{T_m} \quad (11)$$

From the Gibbs–Helmholtz Equation (12), the molar free energy ΔG_{unf} can be calculated, if one assumes ΔH_{unf} and ΔS_{unf} to be temperature-independent

$$\Delta G_{\mathrm{unf}} = \Delta H_{\mathrm{unf}} - T\Delta S_{\mathrm{unf}} \quad (12)$$

Mg^{2+}-dependence of the RNA melting point T_m

The RNA melting point T_m can be determined by CD spectroscopy. Assuming $T_m([Mg])$ to be linearly dependent on the fraction of RNA bound to Mg^{2+} [Equation (13)], the free energy ΔG_{CD} of Mg^{2+} binding to the RNA can be calculated according to Equation (14):

$$T_{\mathrm{m}}([\mathrm{Mg}^{2+}]) = T_{\mathrm{m}}^{\mathrm{no\,Mg}} + \Delta T_{\mathrm{m}} = T_{\mathrm{m}}^{\mathrm{no\,Mg}} + \Delta T_{\mathrm{m,max}}[\mathrm{RNA_{bound}}]/[\mathrm{RNA_{total}}] \quad (13)$$

$$T_{\mathrm{m}}\left(\left[\mathrm{Mg}^{2+}\right]\right) = T_{\mathrm{m}}^{\mathrm{noMg}} + \frac{\Delta T_{\mathrm{m,max}}\left[\mathrm{Mg}^{2+}\right]}{\exp(\Delta G_{\mathrm{CD}}/(\mathrm{RT})) + \left[\mathrm{Mg}^{2+}\right]} = T_{\mathrm{m}}^{\mathrm{noMg}} + \frac{\Delta T_{\mathrm{m,max}}\left[\mathrm{Mg}^{2+}\right]}{K_{\mathrm{CD}} + \left[\mathrm{Mg}^{2+}\right]} \quad (14)$$

In Equation (14), T_m is the melting point of the RNA, T_m^{noMg} is the melting point in the absence of Mg^{2+} ions, $\Delta T_{m,max}$ is the maximal change in T_m caused by Mg^{2+}, $[Mg^{2+}]$ is the Mg^{2+} concentration, K_{CD} is the RNA:Mg^{2+} dissociation constant and ΔG_{CD} is the free energy of Mg^{2+} binding.

bgaB reporter gene assay

Three different translational fusion constructs have been used to study the temperature dependence of gene expression in *E. coli* using the ß-galactosidase gene *bgaB* as reporter. Constructs were designed by introducing the temperature sensitive hairpin 2 of the 5′-UTR of the *Salmonella agsA* gene in front of the heat stable ß-galactosidase gene *bgaB* utilizing an EcoRI restriction site (underlined in the sequences).

The 4U-hp2-wt construct contains the second hairpin of the fourU (4U) RNA thermometer (41) in an optimized vector. Sequence: aGCGTTGAACTTTTGAATAGTGA TTCAGGAGGTTAATGATGGCAGAATTC∼*bgaB*.
The 4U-hp2-A8C-mutant construct differs from the wild-type construct by an A to C mutation (highlighted boldly). Sequence: aGCGTTGA**C**CTTTTGAATAGTGA TTCAGGAGGTTAATGATG GCAGAATTC∼*bgaB*.
In the 4U-hp2-G14A-C25U-mutant the G14-C25 base pair is exchanged to an A14-U25 base pair (highlighted boldly). Sequence: aGCGTTGAACTTTT**A**AATAGTGA TT**T**AGGAGGTTAATGATGGCAGAATTC∼*bgaB*.
An amount of 25 ml LB-Amp (150 µg/ml), pre-warmed in a shaker to 30°C were inoculated with 1.5 ml over night culture (5 ml grown at 30°C) of DH5α cells containing the plasmids. Cells were grown to an optical density (OD_{600}) of 0.5. After induction of transcripts with 25 µl L-arabinose (10%), 8 ml of the culture were shifted to two pre-warmed, shaking flasks at different temperatures, respectively. After 30 min cells were used for the enzymatic assay as described before (47). To compare the different measurements the expression value for the wt at 30°C was set to 1, respectively.

RESULTS AND DISCUSSION

Hairpin stability of the fourU thermometer inversely correlates with gene expression

In our previous study, we determined base-pair stabilities of hairpin 2 (4U-hp2-wt, Figure 2B), which represents the temperature responsive hairpin of the *Salmonella* fourU thermometer, in comparison with a stabilized point mutant (4U-hp2-A8C-mutant), in which the AG mismatch of the wt structure was replaced by a CG pair (Figure 2A). From this study, we concluded that the G14–C25 base pair is by far the most stable base pair in the thermometer hairpin and has a stabilizing effect on the secondary structure of the entire RNA helix (39). Thus, substitution of this stable GC base pair into a less stable AU base pair (Figure 2C) is predicted to result in a significant reduction of the thermal stability of the 4U-hp2 RNA. CD unfolding curves recorded on the G14A–C25U double mutant indeed confirmed the expected behavior (Figure 3A). The GC to AU exchange resulted in a melting point T_m of 35.9°C, which is 5.2°C lower than the T_m value of the wild-type RNA and 16.3°C lower than the 4U-hp2-A8C mutant RNA (Figure 3A and B). T_m values for the three RNAs under investigation are given in Table 1.

Reversible melting and refolding of an RNA thermometer has recently been shown to be physiologically important for fitness of a cyanobacterium (48). CD unfolding and refolding curves demonstrated a similar full reversibility of the unfolding transition of all three fourU hairpins investigated in the current study since start and end points of unfolding and refolding curves are identical (Supplementary Figures S1–S3). However, unfolding and refolding curves slightly differ due to disturbance of the equilibrium caused by the continuous temperature change during the temperature scan. For the subsequent analysis, melting and refolding curves were averaged (the averaged curve will be referred to as unfolding curve from now on) to derive the unfolding curve under equilibrium conditions. Unfolding curves were normalized according to Equation (9) and $\alpha(T)$ values were determined assuming a two–state model (folded; unfolded) for RNA unfolding. The thermodynamic parameters ΔH_{unf}, ΔS_{unf} and ΔG_{unf} were derived according to Equations (10–12) from the $\alpha(T)$ curves shown in Figure 3A. ΔH_{unf}, ΔS_{unf}, ΔG_{unf} and T_m values for the three RNAs under investigation are given in Table 1.

From the ΔH_{unf} and ΔS_{unf} values, the corresponding $\Delta G_{unf}(T)$ curves can be calculated according to the Gibbs–Helmholtz equation. These $\Delta G_{unf}(T)$ curves are illustrated for the wild-type RNA and the two mutants in Figure 3B. Remarkably, all three $\Delta G_{unf}(T)$ curves exhibit an intersection point at $T_c = 81.8$°C. At this temperature, the three RNAs possess the same stability $\Delta G_{unf}(81.8°C) = -31.94$ kJ/mol. At T_c, the unfolded RNA is almost exclusively populated since it is then much more stable than the folded conformation. The

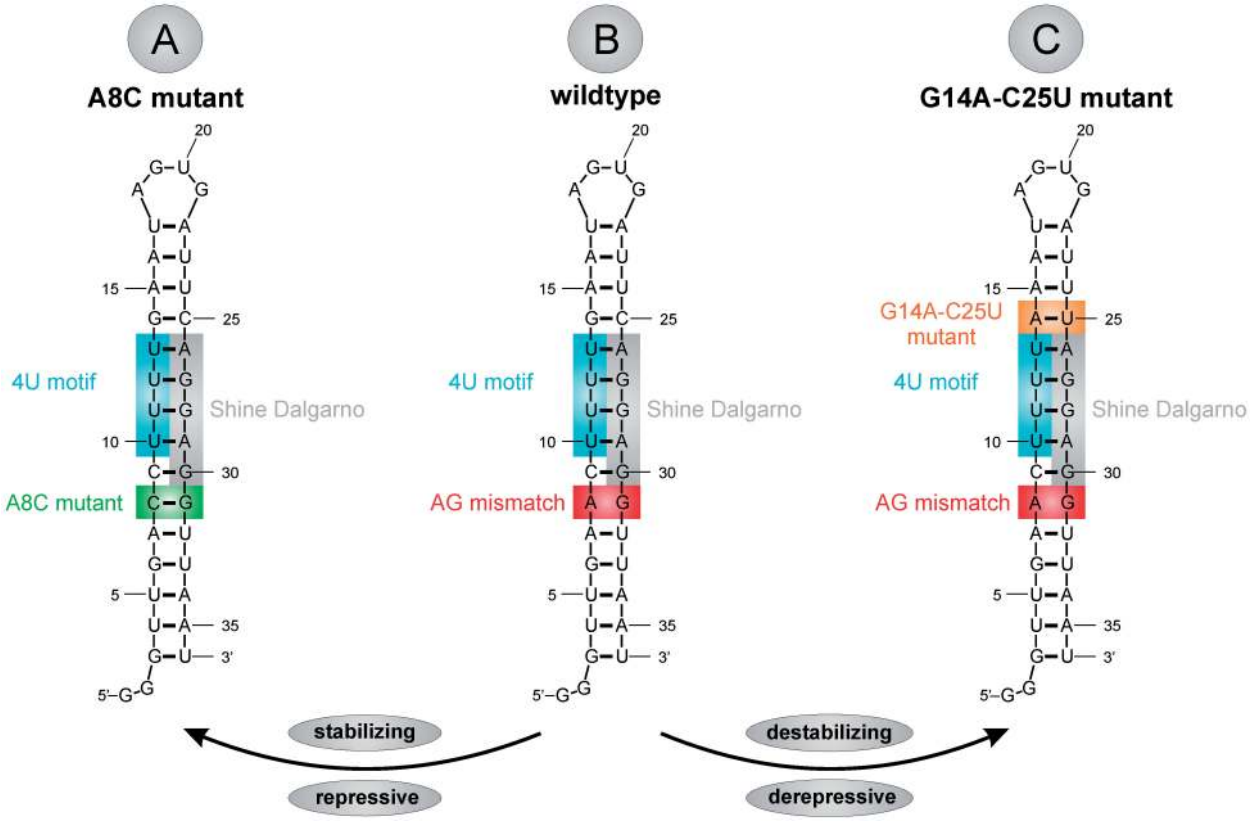

Figure 2. Sequence and secondary structure of hairpin 2 of the *Salmonella* fourU RNA thermometer and mutants used in this study. (**A**) Secondary structure of the 4U-hp2-A8C mutant RNA. (**B**) Secondary structure of the 4U-hp2-wt RNA. (**C**) Secondary structure of the 4U-hp2-G14A-C25U mutant RNA.

existence of an intersection point of the $\Delta G_{unf}(T)$ curves is a consequence of the linear enthalpy–entropy correlation of the global unfolding transition which is depicted in Figure 3C. The slope of the $\Delta H_{unf}(\Delta S_{unf})$ correlation is equal to $m = 354.9\,K$ and the ordinate intercept was determined to be $y0 = -31.95 \pm 0.95\,kJ/mol$. Linear enthalpy–entropy correlations for global unfolding transitions have been reported earlier by Searle and Williams (49) and by Petruska (50) for DNA duplexes. There is also a strong linear correlation between ΔG_{unf} and ΔH_{unf} (Figure 3D) in the fourU RNA thermometer. The slope of this correlation is temperature-dependent and is illustrated for a temperature of 20°C.

Insertion of the enthalpy–entropy correlation into the Gibbs–Helmholtz equation results in the following equation:

$$\Delta G_{unf} = (m - T) \times \Delta S_{unf} + y0 \quad (15)$$

At the compensation temperature (T_c = m), enthalpy and entropy contributions of the RNA-solvent interaction cancel each other and only the RNA–RNA interactions remain and equal $y0$.

Helix unfolding can be approximated according to Searle and Williams (49) by the following equation

$$\Delta G_{unf} \approx \Delta H_{stacking} - T \times \Delta S_{rotation} \quad (16)$$

At T_c, this leads to the following relation

$$\Delta G_{unf}(T_c) = y0 \approx \Delta H_{stacking} - T \times \Delta S_{rotation} \quad (17)$$

$\Delta G_{unf}(T_c)$ is affected by the increase in entropy upon unfolding, mainly caused by the gain of rotational freedom in the RNA backbone $\Delta S_{rotation}$ and the loss of stacking interactions between neighboring nucleobases $\Delta H_{stacking}$. At the compensation temperature T_c, the absolute value of the entropy term $T^*\Delta S$ exceeds by far the absolute value of the enthalpy term $\Delta H_{stacking}$. Thus, the RNA is almost completely unfolded at T_c ($\Delta G_{unf}(T_c) = y0 = -31.95 kJ/mol \pm 0.95 kJ/mol$).

In order to test whether the *in vitro* observations correlate with translational control *in vivo*, the 4U-hp2-wt RNA, the 4U-A8C RNA and the 4U-G14A-C25U RNA were analyzed in the *bgaB* reporter gene assay as described previously (41). The 5′-UTRs were cloned 5′-upstream of the *bgaB* reporter gene downstream of an arabinose-inducible promoter and transformed into *E. coli* DH5α cells. Transcription was initiated with 0.01% (w/v) of L-arabinose and translation at various temperatures was followed by determination of β-galactosidase activity. Expression levels were normalized to the expression of the 4U-hp2-wt sequence at 30°C. The gene expression curves were consistent with the *in vitro* data in that the least stable G14A–C25U mutant led to derepressed, permanently elevated reporter gene expression even at low temperatures (Figure 4). The wild-type 5′-UTR allowed intermediate gene expression at elevated temperatures whereas the stable A8C mutant blocked gene expression completely. The combined *in vivo* and *in vitro* results show

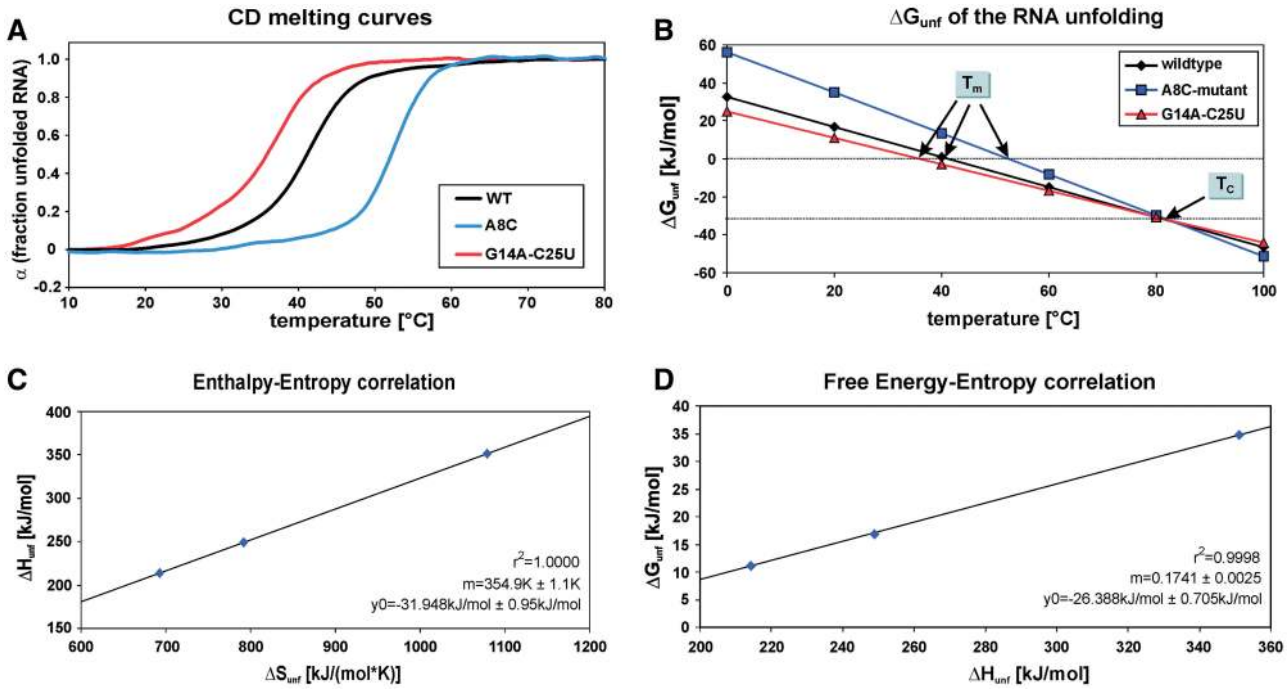

Figure 3. (**A**) Fraction of unfolded RNA α calculated from the CD melting curves according to Equation (9) of the 4U-hp2-wt RNA (black line), 4U-hp2-A8C mutant RNA (blue line) and the 4U-hp2-G14A-C25U double mutant RNA (red line) (**B**) $\Delta G_{unf}(T)$ curves for the global unfolding of the 4U-hp2-wt RNA (black), A8C mutant RNA (blue) and the 4U-hp2-G14A-C25U double mutant RNA (red). $\Delta G_{unf}(T)$ values were calculated from the corresponding ΔH_{unf} and ΔS_{unf} values (Table 1) according to the Gibbs–Helmholtz equation. T_m indicates the three different melting points ($\alpha = 0.5$) of the three RNAs, respectively. $T_c = 354.9$ K represents the compensation temperature at which all three RNAs have the same stability. (**C**) Enthalpy–entropy correlation for the global RNA unfolding determined from the three 4U-hp2 RNAs under investigation. (**D**) Free energy–entropy correlation of the global RNA unfolding ($T = 20°C$) determined for the three 4U-hp2 RNAs analyzed. Linear correlations in (C) and (D) were fitted according to the linear equation $f = y0 + mx$. Fitting results are represented within the figures (C) and (D), respectively.

Table 1. Thermodynamic parameters ΔH_{unf}, ΔS_{unf}, ΔG_{unf} ($T = 20°C$) and T_m for the global unfolding of the 4U-hp2-wt, 4U-hp2-A8C-mutant and 4U-hp2-G14A-C25U-mutant RNAs

	ΔH_{unf} (kJ/mol)	ΔS_{unf} [J/(mol*K)]	ΔG_{unf} (kJ/mol) ($T = 20°C$)	T_m (°C)
Wild-type	248.9	792.0	16.75	41.1
G14A-C25U mutant	214.2	692.9	11.05	35.9
A8C mutant	351.1	1079	34.81	52.2

that seemingly minor mutational alterations can have a very significant effect on RNA stability and functionality of a regulatory RNA element. By switching from the stable A8C sequence to the unstable G14A–C25U sequence, gene expression levels can be increased by factors up to 150. In addition, the wild-type RNA as well as the G14A–C25U RNA are able to induce gene expression in response to a temperature shift from 30°C to 42°C by factors of 8.6 (wt) and 3.9 (mut) (Figure 4). Induction factors of at least 3.5 are described for functional thermoregulators (48,51–53) and an overall enhanced reporter gene expression for mutants with slightly destabilized structures has also been observed for the *ibpA* thermometer from *E. coli* (51). Therefore both *agsA*-5′-UTR-variants, wild-type and G14A–C25U, consisting only of the second hairpin of the natural occurring *agsA* thermometer, work well as control elements in the physiological range of living cells. We observed correlation between hairpin stability determined *in vitro* and gene repression levels measured *in vivo*. Interestingly, gene expression levels start to increase at temperatures significantly lower than the melting point determined *in vitro*. Apparently, translation initiation already occurs even at temperatures where only a minor fraction of RNA thermometers are unfolded.

Curvatures of the temperature dependent gene expression curves *in vivo* (Figure 4) differ from the CD unfolding curves measured *in vitro* (Figure 3A and B). Additional effects to the accessibility of the SD sequence seem to modify the gene expression *in vivo*. Other possible factors like the temperature dependence of transcription, RNA degradation or translation initiation may have additional modulating effects that superimpose the initial RNA thermometer effect.

Mg^{2+}-dependence of the melting point

One well-known factor that contributes to folding of complex RNA structures is Mg^{2+}. In addition, based on the sequence of the fourU thermometer, a Mg^{2+} binding site can be predicted (32). To examine whether this ion plays a structural and functional role in the fourU thermometer, we monitored the Mg^{2+} dependence of the melting

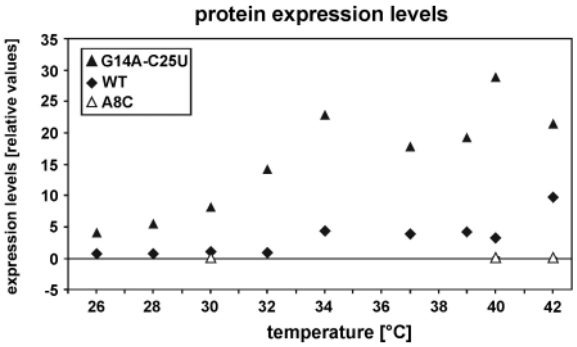

Figure 4. Temperature dependent expression of the agsA-(4U-hp2)-bgaB fusion in DH5α *E. coli* cells. Following RNA constructs were investigated: 4U-hp2-wt (filled diamonds), 4U-hp2-A8C-mutant (open triangles), 4U-hp2-G14A-C25U (filled triangles). Expression levels were referenced to the respective expression level of the 4U-hp2-wt at 30°C which was set to 1.

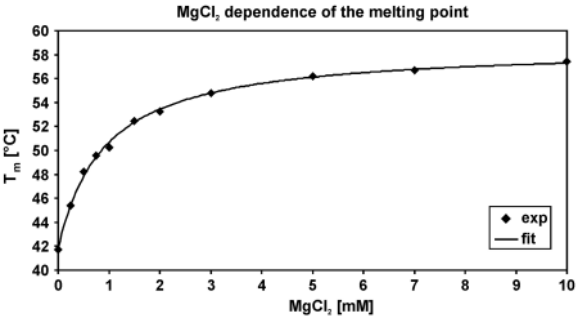

Figure 5. T_m melting point dependence of the 4U-hp2-wt RNA on the $MgCl_2$ concentration. Data points are given as filled diamonds while the fit according to Equation (14) is illustrated as continuous line.

Table 2. Fitting results of the $T_m(Mg^{2+})$ dependence of the 4U-hp2-wt RNA according to Equation (14)

4U-hp2-wt	T_m^{noMg} (°C)	$\Delta T_{m,max}$ (°C)	K_{CD} (μM)	ΔG_{CD} (kJ/mol)
	41.77 ± 0.22	16.93 ± 0.25	899[a] ± 47.9	−18.860 ± 0.14

[a]K_{CD} was calculated for a temperature of 50.24°C. Errors are derived from the fit.

point T_m of the 4U-hp2-wt RNA by CD spectroscopy. The $T_m(Mg^{2+})$ dependence was fitted by Equation (14) (Figure 5) and ΔG_{CD}, $\Delta T_{m,max}$ and T_m^{noMg} values were derived (Table 2).

The $T_m(Mg^{2+})$ dependence can be described by a model which assumes only a single binding site. NMR experiments, however, provide evidence for two Mg^{2+} binding sites (see below). Since Mg^{2+} binding to these sites is cooperative (see below), the 4U-hp2-wt RNA exists most prominently in either the free form or the ternary complex ($[Mg^{2+}*RNA*Mg^{2+}]$) but rarely in one of the binary complexes ($[Mg^{2+}*RNA]$ or $[RNA*Mg^{2+}]$). Thus, the $T_m(Mg^{2+})$ curve exhibits hyperbolic shape and the ΔG_{CD} value determined from the $T_m(Mg^{2+})$-dependence represents the free binding energy between free RNA and ternary $[Mg^{2+}*RNA*Mg^{2+}]$ complex. In addition, we can show that the temperature dependence of T_m is caused by specific and not by diffuse Mg^{2+} binding (Supplementary Data: Evidence for defined Mg^{2+} binding). The fact that the temperature dependence is dominated by defined Mg^{2+} binding does not rule out the possibility of additional diffuse binding. However, according to our data the effects of diffuse Mg^{2+} binding are small in comparison to the effects caused by specific binding, at least in the concentration range observed here (0–7 mM).

The Mg^{2+} dependence of T_m observed *in vitro* indicates a potential effect of fluctuating Mg^{2+} concentrations within the cell on expression levels of genes under the control of the fourU RNA thermometer. According to the literature, the free intracellular Mg^{2+} concentration may vary between 1 and 2 mM (14,18). Such a shift in Mg^{2+} concentration causes a shift of the T_m value of the 4U-hp2-wt RNA by 2.8°C (Figure 5). Thus, varying Mg^{2+} concentration will most probably have a modulating temperature-independent effect on RNA-thermometer-controlled gene expression *in vivo*.

Localization of the Mg^{2+} binding sites

We applied different NMR methods to identify Mg^{2+} binding sites in the 4U-hp2-wt RNA. First, a NOESY experiment of a 4U-hp2-wt RNA sample in the presence of $[Co(NH_3)_6]^{3+}$ ions was performed to identify and localize $[Co(NH_3)_6]^{3+}$ binding sites. $[Co(NH_3)_6]^{3+}$ ions serve as mimic for hexahydrated Mg^{2+} ions and therefore map binding sites for outer sphere coordinated Mg^{2+} ions (28,29,32). Second, we analyzed the PRE effects of the imino signals occurring upon the addition of paramagnetic Mn^{2+} ions to the 4U-hp2-wt RNA sample (28,29). The fact that substoichiometric amounts of Mn^{2+} are sufficient to cause significant line broadening of imino signals in close proximity to Mg^{2+} binding sites reveals that Mg^{2+} ions are in rapid exchange with free divalent ions. The use of Mn^{2+} as probe for Mg^{2+} is supported by the observation that 76% of the intracellular Mg^{2+} ions in prokaryotes (*E. coli*) can be substituted by Mn^{2+} ions without severely impairing viability of the cells (18). Third, we followed CSPs of the imino signals during Mg^{2+} titration experiments (28,29). Fitting of the obtained CSP curves was performed to derive K_D values for Mg^{2+} binding. By taking the results of these three complementary techniques into account, it became possible to unravel the different effects on how Mg^{2+} ions interact with the 4U-hp2-wt RNA. Combination of the information yields a consistent overall picture on the effects of Mg^{2+} ions on the 4U-hp2-wt RNA.

The imino region of the 2D-^{1}H-^{1}H NOESY spectrum of the 4U-hp2-wt RNA in the presence of 5 mM $[Co(NH_3)_6]^{3+}$ ions is given in Figure 6. Protons from $[Co(NH_3)_6]^{3+}$ exhibit strong cross peaks to the imino protons of the nucleobases U11, U12, G27 and/or G28 and weak cross peaks to the imino protons of the adjacent nucleobases U10 and U13. Thus, a binding site for $[Co(NH_3)_6]^{3+}$ is located in close proximity to the nucleobases U11, U12, G27 and G28, most probably in

the major groove of the RNA helix very similar to the binding site described for the structure of the P5b hairpin of the group I intron by Kieft and Tinoco (32).

PRE effects of the imino signals caused by the addition of Mn^{2+} ions were analyzed in order to reveal divalent cation binding sites. For that purpose, [^{1}H,^{15}N]-HSQCs of the imino region of the 4U-hp2-wt RNA sample were recorded and line shapes and intensities of the imino signals were analyzed to quantify the PRE effects. Changes in line widths and signal intensities caused by the addition of 4 μM Mn^{2+} are given in Figure 7. Large PRE effects were observed for the nucleobases U11 and U12 within the RNA helix. In addition, the nucleobases U13, G14 and U33 also show significant PRE effects, while the imino signal of nucleobase U10 exhibits only a very weak PRE effect. Interestingly the G27/G28 double signal only shows a moderate PRE effect in comparison to U11, U12 and U13 which is consistent with binding of $[Co(NH_3)_6]^{3+}$ in the major groove.

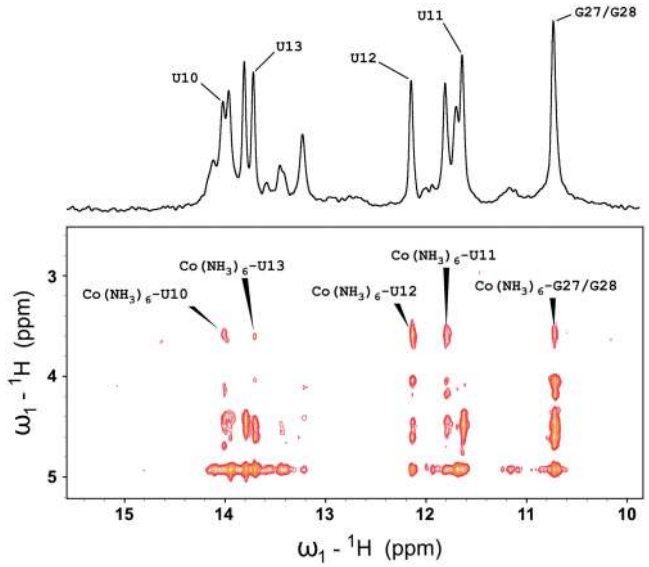

Figure 6. Section from the 2D-^{1}H NOESY experiment performed on a 0.9-mM 4U-hp2-wt RNA sample in the presence of 5 mM $[(Co(NH_3)_6]^{3+}$. Assignments of cross signals between protons of the $[Co(NH_3)_6]^{3+}$ and the imino protons of the RNA are given within the spectrum. On top of the NOESY spectrum, the corresponding imino region of the ^{1}H-1D NMR spectrum is given. Buffer conditions: 15 mM $K_xH_yPO_4$ (pH 6.5), 25 mM KCl, 90% H_2O and 10% D_2O.

Taken together, the PRE analysis reveals the existence of a Mn^{2+} binding site within the 4U-hp2-wt RNA which is located in close proximity to the nucleobases U11, U12 and U13. This Mn^{2+} binding site represents a strong indication for the existence of a Mg^{2+} binding site at exactly the same position within the 4U-hp2-wt RNA. Furthermore, PRE analysis and $[Co(NH_3)_6]^{3+}$ NOESY data reveal binding sites in the same region of the RNA leading to the conclusion that there is one specific outer sphere Mg^{2+} binding site within the fourU motif of the 4U-hp2-wt RNA. Moderate PRE effects of the nucleobases G27/G28 are in agreement with localization of this binding site within the major groove.

Finally, we titrated 4U-hp2-wt RNA with Mg^{2+} ions and analyzed the occurring CSPs of the imino group region within the [^{1}H,^{15}N]-HSQC spectra. CSP([Mg^{2+}]) curves were fitted according to Equation (2) and K_D values were derived. Figure 8 shows Mg^{2+}-dependent CSPs of the imino groups with their respective fits (continuous lines). In Figure 8D, the shifting signals of the imino groups U5 and U13 within the [^{1}H-^{15}N]-HSQC during the titration of the RNA with $MgCl_2$ are shown exemplarily. Fitting results are summarized in Supplementary Table S1. Interestingly, different

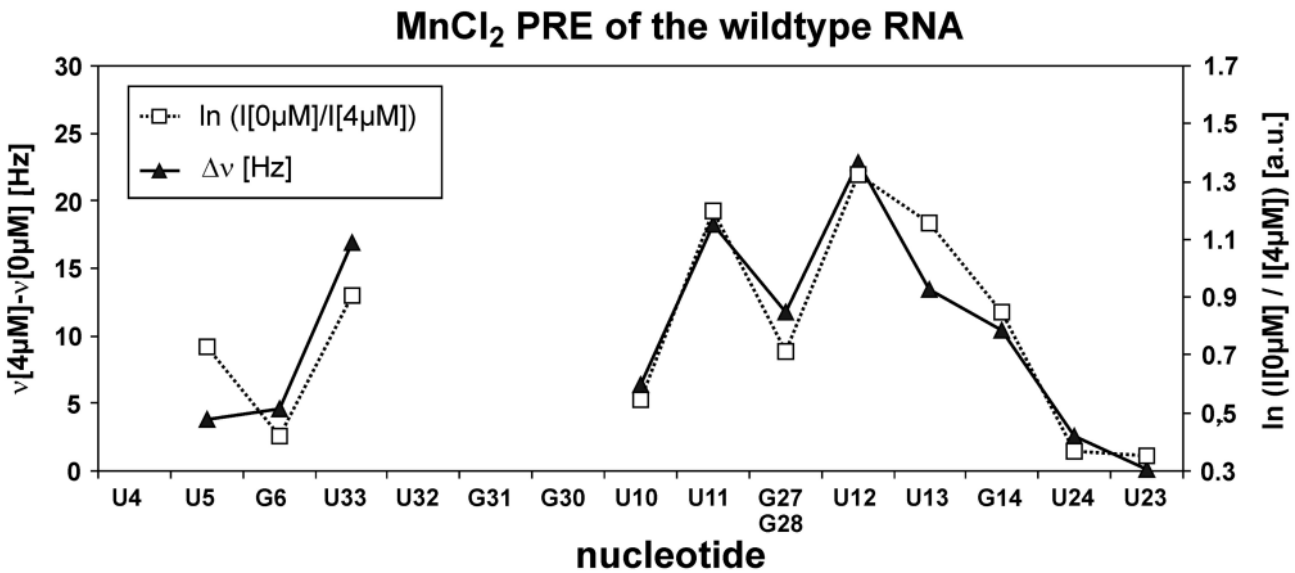

Figure 7. PRE of the imino resonances of the 4U-hp2-wt RNA observed upon the addition of 4 μM $MnCl_2$. Changes in line widths Δν [Hz] in the ^{15}N-dimension are illustrated as filled triangles (continuous line) with the corresponding scale on the left hand side of the diagram and changes in intensity (ln(I[0 μM]/I[4 μM]) [a.u.]) are illustrated as open squares (dotted line) with the corresponding scale on the right hand side. U32 and G31 do not give rise to any observable imino signals and the imino signals of G30 and U4 are too weak to be analyzed.

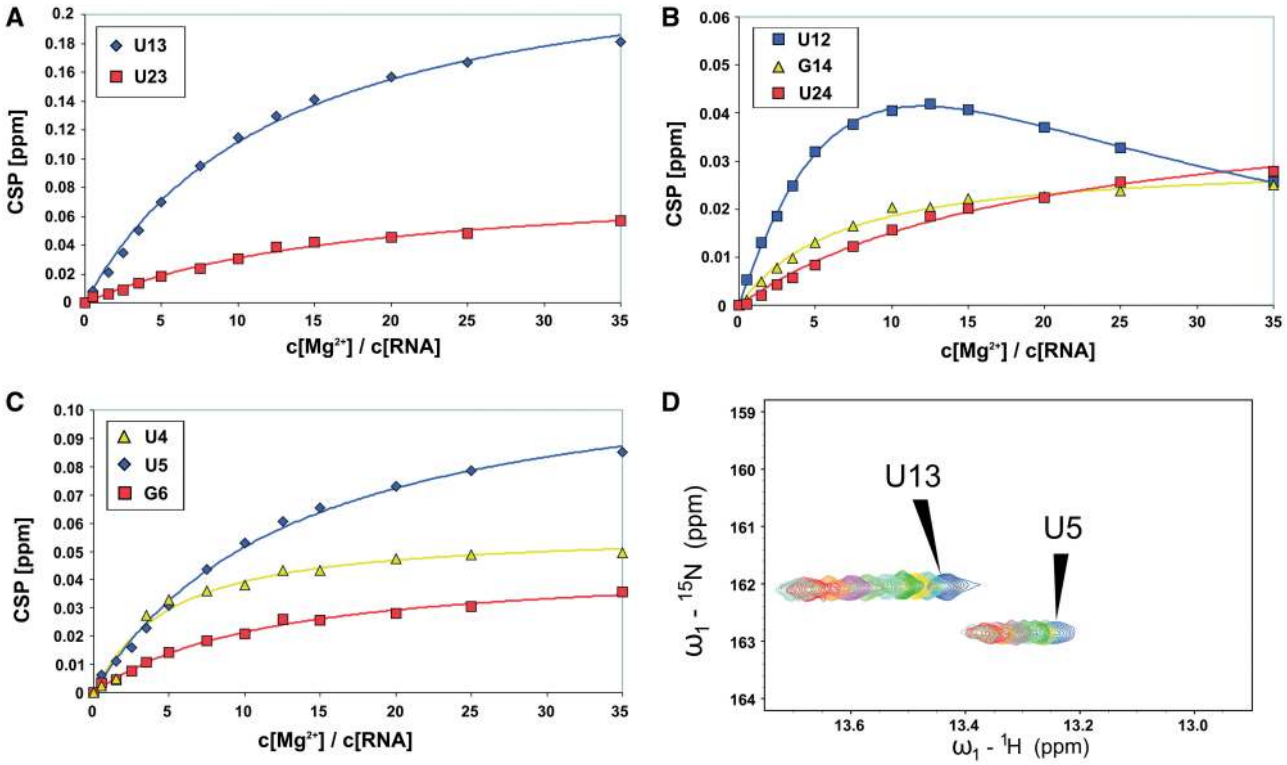

Figure 8. (**A–C**) CSPs of the imino resonances of the nucleobases U13, U23, G14, U24, U4, U5 and G6 plotted against the $[Mg^{2+}]/[RNA]$ ratio and fitted according to Equation (2) (continuous lines). CSPs of the imino signal U12 (B) were fitted by Equation (3) (**D**) Mg^{2+}-dependent changes (CSPs) of the imino groups U13 and U5 within the $[^{1}H,^{15}N]$-HSQC spectrum (titration steps: see 'Materials and Methods' section).

K_{diss} values are obtained for different imino signals. Lowest K_{diss} values are found for U4 (0.85 ± 0.18) and G14 (1.17 ± 0.12 mM). Nucleotides U5, G6 and U13 exhibit K_{diss} values of around 2.34 mM and the nucleotides U23 and U24 show K_{diss} values of ~3.56 mM. U13 shows by far the largest CSP_{max} value (0.250 ± 0.008 ppm).

Multiple conformations of a $[RNA*Mg^{2+}]$-complex assuming only a single Mg^{2+} binding site fail to explain the observed diversity in K_{diss} values as explained in the Supplementary Data (Mg^{2+} binding model for one binding site but different conformations of the $[RNA*Mg^{2+}]$ complex).

In addition, the CSP curve of U12 shows a distinct biphasic behavior. We argue that this behavior can only be explained by two different Mg^{2+} binding sites. The model describing the binding properties of an RNA molecule with two different Mg^{2+} binding sites is given in Figure 1. The dissociation constants derived from the biphasic fit (CSP curve of U12) can be assigned to the macroscopic dissociation constants K_1 (3.58 mM) and K_2 (2.06 mM). Since the observed CSP curves cannot be explained by negative cooperativity (negative cooperativity would lead to negative microscopic dissociation constants), cooperativity has to be positive. In such model, the smallest dissociation constants derived by monophasic fitting have to be purely monophasic and correspond to one of the microscopic dissociation constants $K_{2,4}$ and $K_{3,4}$. Thus, $K_{2,4}$ was set to 1.17 ± 0.12 mM (G14) and $K_{3,4}$ to 0.85 ± 0.18 mM (U4) as derived from monophasic fitting of the CSP curves (Figure 8 and Supplementary Table S1). However, an assignment of the microscopic dissociation constant $K_{2,4}$ (1.17 mM) or the microscopic dissociation constant $K_{3,4}$ (0.89 mM) to the outer sphere Mg^{2+} binding site within the fourU motif is not possible. According to the equations connecting the different dissociation constants (Figure 1), the microscopic dissociation constants $K_{1,2}$ and $K_{1,3}$ could be derived (Table 3). Free energy values for Mg^{2+} binding ΔG_{K1} and ΔG_{K2} at a temperature of 10°C as well as the free energy for ternary $[Mg^{2+}*RNA*Mg^{2+}]$ complex formation ΔG_{ges} are given in Table 3.

The macroscopic dissociation constant K_1 is notably larger than K_2 although formation of the binary complex is statistically favored over the formation of the ternary complex. The resulting microscopic dissociation constants connecting the free RNA and the binary complexes $K_{1,2}$ (6.31 mM) and $K_{1,3}$ (8.26 mM) are much larger than the corresponding dissociation constants $K_{2,4}$ (1.17 mM) and $K_{3,4}$ (0.89 mM) connecting the binary complexes with the ternary complex. In other words, binding of one Mg^{2+} ion promotes binding of the second Mg^{2+} ion (positive cooperativity). According to the determined dissociation constants (Table 3), we determine a Hill coefficient $b = 1.47$ (Supplementary Figure S4). This intermediate positive cooperativity is in line with positive cooperativity values for Mg^{2+} binding to $tRNA^{Phe}$ reported in the literature ($b = 1.7$) (54).

Table 3. Thermodynamic parameters of Mg^{2+} binding as well as macroscopic and microscopic dissociation constants of the two-binding-site-model (Figure 1)

	K_{diss} (mM)
K_1	3.58 ± 0.67 mM
K_2	2.06 ± 0.66 mM
$K_{2,4}$	1.17 ± 0.12 mM
$K_{3,4}$	0.85 ± 0.12 mM
$K_{1,2}$	6.31 ± 2.43 mM
$K_{1,3}$	8.68 ± 3.71 mM
ΔG_{K1} (10°C)	−13.262 ± 0.446 kJ/mol
ΔG_{K2} (10°C)	−14.556 ± 0.780 kJ/mol
ΔG_{ges} (10°C)	−27.818 ± 0.899 kJ/mol
ΔG_{CD} (50.24°C)	−18.860 ± 0.143 kJ/mol
ΔG_{ges} (37°C)	−21.807 ± 0.443 kJ/mol
ΔH_{ges}	−90.855 ± 6.469 kJ/mol
$T^*\Delta S_{ges}$ (10°C)	−63.037 ± 6.404 kJ/mol

ΔG_{K1}, ΔG_{K2} and ΔG_{ges} were calculated for a temperature of 10°C. ΔG_{CD} (50.24°C) was derived from CD melting studies. ΔH_{ges}, $T^*\Delta S_{ges}$ and ΔG_{ges} (37°C) were calculated from the difference of ΔG_{ges} (10°C) and ΔG_{CD} (50.24°C). Errors in K_1, K_2, $K_{2,4}$, $K_{3,4}$ and K_{CD} (Table 2) are statistical errors resulting from the fit. Errors in $K_{1,2}$, $K_{1,3}$, ΔG_{K1} (10°C), ΔG_{K2} (10°C), ΔG_{ges} (10°C), ΔG_{CD} (50.24°C), ΔH_{ges} and $T^*\Delta S_{ges}$ (10°C) are Gaussian errors calculated by error propagation.

A description how two Mg^{2+} binding sites may lead to the observed variety of monophasic CSP curves is given in the Supplementary Data (Qualitative explanation of the observed CSP curves using a two binding site model).

From the Mg^{2+} dependence of the melting point T_m determined by CD spectroscopy (Figure 5 and Table 2), the free energy for Mg^{2+} binding ΔG_{CD} at a temperature of 50.24°C was determined. Assuming that Mg^{2+} only binds to the folded but not to the unfolded RNA ΔG_{CD} is equal to ΔG_{ges}. From the difference of ΔG_{ges} ($T = 10$°C) and ΔG_{CD} ($T = 50.24$°C), ΔH_{ges} and $T^*\Delta S_{ges}$ (10°C) were calculated according to the Gibbs–Helmholtz equation assuming that ΔH_{ges} and ΔS_{ges} are not temperature-dependent. Results are given in Table 3.

The $T^*\Delta S_{ges}$ value (−63.037 ± 6.404 kJ/mol) indicates that the Mg^{2+}-bound state exhibits a higher degree of order than the free RNA which appears reasonable since in the ternary [Mg^{2+}*RNA*Mg^{2+}] complex, rotational and translational degrees of freedom of the hexahydrated Mg^{2+} ions are reduced. In particular, binding of two hexahydrated Mg^{2+} ions to the RNA molecule is accompanied by the loss of three rotational and three translational degrees of freedom per hexahydrated Mg^{2+} ion while the loss of one degree of freedom reduces the entropy by ½ R. However, this accounts only for 50 J/(mol*K) (2*6/2*R) which is far less than the observed change in entropy ($\Delta S_{ges} = 223 \pm 23$ J/(mol*K)). Thus, additional entropy reducing effects have to be present. Such effects might be caused by an increased conformational restriction of the RNA itself or by a higher degree of order in the water molecules involved. This energetically unfavorable entropy term is overcompensated by stabilizing ΔH_{ges} contributions (−90.855 ± 6.469 kJ/mol) which most probably result from energetically favorable Coulomb interactions.

Using ΔG_{CD} (50.24°C) and ΔG_{ges} (10°C) values (Table 3), the free energy for Mg^{2+} binding ΔG_{ges} (37°C) calculates to −21.807 ± 0.443 kJ/mol. Such value indicates that most probably not more than two Mg^{2+} binding sites are involved since three or more Mg^{2+} binding sites would lead to a lower ΔG_{ges} value or to K_{diss} values higher than those reported for diffuse binding (55). It may be noticed that the average ΔG_{ges} value that we obtained per magnesium binding site (−10.9 kJ/mol) is in surprisingly good agreement with the average value (∼–11 kJ/mol) that can be derived from the difference in concentration of bound and free magnesium *in vivo* (13,14).

In summary, these results indicate the existence of two Mg^{2+} binding sites within the 4U-hp2-wt RNA. At least one of these binding sites is outer sphere coordinated and is located in proximity to the nucleobases U11, U12, G27 and G28 most probably within the major groove of the RNA. Although the existence of a second Mg^{2+} binding site is certain, it could not be localized unambiguously. PRE experiments suggest that it is near the nucleobase U33 (Figure 7). The fact that only one binding site could be located with $[Co(NH_3)_6]^{3+}$ suggests that the second Mg^{2+} binding site might be inner sphere coordinated. However, it is also possible that the two binding sites are in such close proximity that they cannot be identified as two independent binding sites.

Using a combination of *in vitro* and *in vivo* experiments we show that fourU RNA thermometers are optimized in their sequence and Mg^{2+} binding properties. Two Mg^{2+} binding sites with positive cooperativity could be identified within the 4U-hp2-wt RNA, one of them as outer sphere binding site directly within the fourU motif as predicted from the secondary structure of this RNA (32). Mg^{2+} concentration has a modulating effect on the melting point of the fourU RNA thermometer and therefore most probably influences gene expression *in vivo*. From the *in vivo* experiments it became obvious that the onset of gene expression already occurs at temperatures significantly below the melting point. Apparently, a small fraction of RNA thermometers in the open conformation seems to be sufficient to efficiently permit translation initiation. In addition, the *in vivo* experiments reveal that already small changes in the temperature dependent stability (T_m) of the RNA thermometer lead to tremendous effects on gene expression of the downstream gene.

SUPPLEMENTARY DATA

Supplementary Data are available at NAR Online.

ACKNOWLEDGEMENTS

The authors thank one reviewer for the interesting and constructive discussions.

FUNDING

State of Hesse (Center for Biomolecular Magnetic Resonance, BMRZ); DFG (priority program SPP 1258: Sensory and regulatory RNAs in prokaryotes). H.S. is

member of the DFG-funded Cluster of Excellence: Macromolecular complexes. Funding for open access charge: DFG.

Conflict of interest statement. None declared.

REFERENCES

1. Walker,G.M. (1994) The roles of magnesium in biotechnology. *Crit. Rev. Biotechnol.*, **14**, 311–354.
2. Wood,J.M. (2007) Bacterial osmosensing transporters. *Meth. Enzymol.*, **428**, 77–107.
3. Shiman,R. and Draper,D.E. (2000) Stabilization of RNA tertiary structure by monovalent cations. *J. Mol. Biol.*, **302**, 79–91.
4. Pyle,A.M. (2002) Metal ions in the structure and function of RNA. *J. Biol. Inorg. Chem.*, **7**, 679–690.
5. Merlevede,W., Vandenheede,J.R., Goris,J. and Yang,S.D. (1984) Regulation of ATP-Mg-dependent protein phosphatase. *Curr. Top. Cell. Regul.*, **23**, 177–215.
6. Brock,T.D. (1962) Effects of magnesium ion deficiency on *Escherichia coli* and possible relation to the mode of action of Novobiocin. *J. Bacteriol.*, **84**, 679–682.
7. Hughes,M.N. and Poole,R.K. (1989) *Metals and Microorganisms*. Chapman and Hall, London.
8. Meers,J.L. and Tempest,D.W. (1969) The influence of extracellular products on the behaviour of mixed microbial populations in magnesium-limited chemostat cultures. *J. Gen. Microbiol.*, **52**, 309–317.
9. Klein,D.J., Moore,P.B. and Steitz,T.A. (2004) The contribution of metal ions to the structural stability of the large ribosomal subunit. *RNA*, **10**, 1366–1379.
10. Tempest,D.W. and Strange,R.E. (1966) Variation in content and distribution of magnesium, and its influence on survival, in *Aerobacter aerogenes* grown in a chemostat. *J. Gen. Microbiol.*, **44**, 273–279.
11. Webb,M. (1968) The influence of certain trace metals on bacterial growth and magnesium utilization. *J. Gen. Microbiol.*, **51**, 325–335.
12. Hurwitz,C. and Rosano,C.L. (1967) The intracellular concentration of bound and unbound magnesium ions in *Escherichia coli*. *J. Biol. Chem.*, **242**, 3719–3722.
13. Moncany,M.L. and Kellenberger,E. (1981) High magnesium content of *Escherichia coli* B. *Experientia*, **37**, 846–847.
14. Alatossava,T., Jutte,H., Kuhn,A. and Kellenberger,E. (1985) Manipulation of intracellular magnesium content in polymyxin B nonapeptide-sensitized *Escherichia coli* by ionophore A23187. *J. Bacteriol.*, **162**, 413–419.
15. Lusk,J.E. and Kennedy,E.P. (1969) Magnesium transport in *Escherichia coli*. *J. Biol. Chem.*, **244**, 1653–1655.
16. Lusk,J.E., Williams,R.J. and Kennedy,E.P. (1968) Magnesium and the growth of *Escherichia coli*. *J. Biol. Chem.*, **243**, 2618–2624.
17. Silver,S. (1969) Active transport of magnesium in *Escherichia coli*. *Proc. Natl Acad. Sci. USA*, **62**, 764–771.
18. Silver,S. and Clark,D. (1971) Magnesium transport in *Escherichia coli*. *J. Biol. Chem.*, **246**, 569–576.
19. Nelson,D.L. and Kennedy,E.P. (1972) Transport of magnesium by a repressible and a nonrepressible system in *Escherichia coli*. *Proc. Natl Acad. Sci. USA*, **69**, 1091–1093.
20. Scribner,H., Eisenstadt,E. and Silver,S. (1974) Magnesium transport in *Bacillus subtilis* W23 during growth and sporulation. *J. Bacteriol.*, **117**, 1224–1230.
21. Hmiel,S.P., Snavely,M.D., Miller,C.G. and Maguire,M.E. (1986) Magnesium transport in *Salmonella typhimurium*: characterization of magnesium influx and cloning of a transport gene. *J. Bacteriol.*, **168**, 1444–1450.
22. Hmiel,S.P., Snavely,M.D., Florer,J.B., Maguire,M.E. and Miller,C.G. (1989) Magnesium transport in *Salmonella typhimurium*: genetic characterization and cloning of three magnesium transport loci. *J. Bacteriol.*, **171**, 4742–4751.
23. Snavely,M.D., Florer,J.B., Miller,C.G. and Maguire,M.E. (1989) Magnesium transport in *Salmonella typhimurium*: expression of cloned genes for three distinct Mg2+ transport systems. *J. Bacteriol.*, **171**, 4752–4760.
24. Snavely,M.D., Florer,J.B., Miller,C.G. and Maguire,M.E. (1989) Magnesium transport in *Salmonella typhimurium*: $^{28}Mg^{2+}$ transport by the CorA, MgtA, and MgtB systems. *J. Bacteriol.*, **171**, 4761–4766.
25. Snavely,M.D., Gravina,S.A., Cheung,T.T., Miller,C.G. and Maguire,M.E. (1991) Magnesium transport in *Salmonella typhimurium*. Regulation of mgtA and mgtB expression. *J. Biol. Chem.*, **266**, 824–829.
26. Basu,S., Rambo,R.P., Strauss-Soukup,J., Cate,J.H., Ferre-D'Amare,A.R., Strobel,S.A. and Doudna,J.A. (1998) A specific monovalent metal ion integral to the AA platform of the RNA tetraloop receptor. *Nat. Struct. Biol.*, **5**, 986–992.
27. Butcher,S.E., Allain,F.H. and Feigon,J. (2000) Determination of metal ion binding sites within the hairpin ribozyme domains by NMR. *Biochemistry*, **39**, 2174–2182.
28. Feigon,J., Butcher,S.E., Finger,L.D. and Hud,N.V. (2001) Solution nuclear magnetic resonance probing of cation binding sites on nucleic acids. *Meth. Enzymol.*, **338**, 400–420.
29. Gonzalez,R.L. Jr and Tinoco,I. Jr (2001) Identification and characterization of metal ion binding sites in RNA. *Meth. Enzymol.*, **338**, 421–443.
30. Fürtig,B., Richter,C., Wöhnert,J. and Schwalbe,H. (2003) NMR spectroscopy of RNA. *Chembiochem*, **4**, 936–962.
31. Martin,R.B. (1990) In Dekker,M. (ed.), *Metal Ions in Biological Systems*, New York.
32. Kieft,J.S. and TinocoI.Jr (1997) Solution structure of a metal-binding site in the major groove of RNA complexed with cobalt (III) hexammine. *Structure*, **5**, 713–721.
33. Jack,K.D., Means,J.A. and Hines,J.V. (2008) Characterizing riboswitch function: identification of Mg2+ binding site in T box antiterminator RNA. *Biochem. Biophys. Res. Comm.*, **370**, 306–310.
34. Buck,J., Noeske,J., Wöhnert,J. and Schwalbe,H. (2010) Dissecting the influence of Mg^{2+} on 3D architecture and ligand-binding of the guanine-sensing riboswitch aptamer domain. *Nucleic Acids Res.*, **38**, 4143–4153.
35. Ramesh,A. and Winkler,W.C. (2010) Magnesium-sensing riboswitches in bacteria. *RNA Biol.*, **7**, 77–83.
36. Winkler,W.C. and Breaker,R.R. (2005) Regulation of bacterial gene expression by riboswitches. *Annu. Rev. Microbiol.*, **59**, 487–517.
37. Schwalbe,H., Buck,J., Fürtig,B., Noeske,J. and Wöhnert,J. (2007) Structures of RNA switches: insight into molecular recognition and tertiary structure. *Angew. Chem. Int. E. Engl.*, **46**, 1212–1219.
38. Narberhaus,F. (2010) Translational control of bacterial heat shock and virulence genes by temperature-sensing mRNAs. *RNA Biol.*, **7**, 84–89.
39. Rinnenthal,J., Klinkert,B., Narberhaus,F. and Schwalbe,H. (2010) Direct observation of the temperature-induced melting process of the *Salmonella* fourU RNA thermometer at base-pair resolution. *Nucleic Acids Res.*, **38**, 3834–3847.
40. Neupert,J., Karcher,D. and Bock,R. (2008) Design of simple synthetic RNA thermometers for temperature-controlled gene expression in *Escherichia coli*. *Nucleic Acids Res.*, **36**, e124.
41. Waldminghaus,T., Heidrich,N., Brantl,S. and Narberhaus,F. (2007) FourU: a novel type of RNA thermometer in *Salmonella*. *Mol. Microbiol.*, **65**, 413–424.
42. Bodenhausen,G. and Ruben,D.J. (1980) Natural abundance nitrogen-15 NMR by enhanced heteronuclear spectroscopy. *Chem. Phys. Lett.*, **69**, 185–189.
43. Sklenar,V., Piotto,M., Leppik,R. and Saudek,V. (1993) Gradient-tailored water suppression for 1H-15N HSQC experiments optimized to retain full sensitivity. *J. Magn. Reson., Series A*, **102**, 241–245.
44. Noeske,J., Schwalbe,H. and Wöhnert,J. (2007) Metal-ion binding and metal-ion induced folding of the adenine-sensing riboswitch aptamer domain. *Nucleic Acids Res.*, **35**, 5262–5273.
45. Stoldt,M., Wöhnert,J., Ohlenschläger,O., Görlach,M. and Brown,L.R. (1999) The NMR structure of the 5S rRNA E-domain-protein L25 complex shows preformed and induced recognition. *EMBO J.*, **18**, 6508–6521.

46. Marky,L.A. and Breslauer,K.J. (1987) Calculating thermodynamic data for transitions of any molecularity from equilibrium melting curves. *Biopolymers*, **26**, 1601–1620.
47. Gaubig,L.C., Waldminghaus,T. and Narberhaus,F. (2011) Multiple layers of control govern expression of the *Escherichia coli* ibpAB heat shock operon. *Microbiology*, **157**, 66–76.
48. Kortmann,J., Sczodrok,S., Rinnenthal,J., Schwalbe,H. and Narberhaus,F. (2011) Translation on demand by a simple RNA-based thermosensor. *Nucleic Acids Res.*, **39**, 2855–2868.
49. Searle,M.S. and Williams,D.H. (1993) On the stability of nucleic acid structures in solution: enthalpy-entropy compensations, internal rotations and reversibility. *Nucleic Acids Res.*, **21**, 2051–2056.
50. Petruska,J. and Goodman,M.F. (1995) Enthalpy-entropy compensation in DNA melting thermodynamics. *J. Biol. Chem.*, **270**, 746–750.
51. Waldminghaus,T., Gaubig,L.C., Klinkert,B. and Narberhaus,F. (2009) The *Escherichia coli* ibpA thermometer is comprised of stable and unstable structural elements. *RNA Biol.*, **6**, 455–463.
52. Morita,M.T., Tanaka,Y., Kodama,T.S., Kyogoku,Y., Yanagi,H. and Yura,T. (1999) Translational induction of heat shock transcription factor sigma32: evidence for a built-in RNA thermosensor. *Genes Dev.*, **13**, 655–665.
53. Nocker,A., Hausherr,T., Balsiger,S., Krstulovic,N.P., Hennecke,H. and Narberhaus,F. (2001) A mRNA-based thermosensor controls expression of rhizobial heat shock genes. *Nucleic Acids Res.*, **29**, 4800–4807.
54. Labuda,D., Nicoghosian,K. and Cedergren,R. (1985) Cooperativity in low-affinity Mg^{2+} binding to tRNA. *J. Biol. Chem.*, **260**, 1103–1107.
55. Laing,L.G., Gluick,T.C. and Draper,D.E. (1994) Stabilization of RNA Structure by Mg Ions - Specific and Nonspecific Effects. *J. Mol. Biol.*, **237**, 577–587.